Journal of Materials Chemistry C

RSC Publishing

PAPER

View Article Online
View Journal | View Issue

Cite this: J. Mater. Chem. C, 2013, 1, 5567

Gold mesoparticles with precisely controlled surface topographies for single-particle surface-enhanced Raman spectroscopy†

Zhen Liu,‡[a] Fangling Zhang,‡[a] Zhongbo Yang,[a] Hongjun You,*[a] Cuifeng Tian,[a] Zhiyuan Li[b] and Jixiang Fang*[a]

Understanding of the influence of nanotextured surface topographies on surface-enhanced Raman scattering (SERS) is still rather limited, even after intensive research in recent years; this is mainly due to the absence of a synthesis system to control the surface morphologies on metal meso-/nanoparticles. Here, a facile particle-mediated aggregation protocol was reported to synthesize a series of uniform gold mesoparticles with a nanotextured rough surface. The surface topographies can be precisely controlled by varying the temperatures and concentrations of dopa and Au ions. For example, the tips can be well changed from half-sphere to spike, and then to blade, and the size of the tips also can be tuned, such that the thickness of the blade-like tips can be artificially controlled from 9 to 14 nm. Single-particle SERS analysis reveals that the uniform Au mesoparticles with highly nanotextured topography have enhancement factors greater than 1.0×10^8 with narrow distribution. The effect of the precisely controlled mesoparticle topographies on SERS properties was deeply studied using Raman analysis and finite-difference time-domain (FDTD) simulation. The result indicated that a strong electric field will be induced at the tips and slits on the flower-like mesoparticle surface by the confined light in the cavities between the petals. As such, the current protocol opens up avenues for the fabrication of structurally reproducible mesosuperstructure-based SERS sensors.

Received 2nd May 2013
Accepted 11th July 2013

DOI: 10.1039/c3tc30824c

www.rsc.org/MaterialsC

1 Introduction

As a powerful and extremely sensitive analytical technique, surface-enhanced Raman scattering (SERS) spectroscopy has attracted great interest for applications in biochemistry, chemical production, and environmental monitoring.[1–5] Since it was first discovered that a rough metal surface could greatly enhance the Raman scattering spectroscopy of adsorbed molecules, with the effect being called SERS,[6] many efforts have been made to explore new substrates with high sensitivity and reproducibility using various synthesis methods or preparation techniques.[7–13] The sensitivity of SERS substrates is mainly determined by electromagnetic enhancement due to localized plasmon resonances in noble or transition metals.[14] The plasmonic coupling effect induces very high local electromagnetic enhancement in certain regions called "hot spots", leading to high SERS enhancement (by more than 10^{10}) that is even plausible for single molecule detection.[15–17] The localized plasmon resonance is influenced by some general factors of the substrates, such as shape, size, and gap distance.[18–20] Additionally, the interaction between light and the substrates at the nanometer scale also has an effect on the SERS properties, such as the wavelength and polarization of the incident light.[20–22]

From the initial rough metal surface obtained by electrochemical corrosion[6] or electrochemical deposition,[23,24] two main classes of SERS substrates have been developed in the past years. One is the substrate that is usually prepared using "top-down" methods, such as electron beam lithography,[7] nanosphere lithography,[9] and electrospinning technique.[8] It is possible to establish large scale production of this type of substrate. Using some techniques, uniform periodic nanostructures can be fabricated. However, current techniques still have difficulties in realizing controllable and highly dense small gaps between metal nanostructures. Thus, only a moderate enhancement (10^5 to 10^6) has been achieved with this kind of substrate.[25] The other is nanoparticle colloids, such as Ag or Au nanoparticles with sizes of 50–100 nm.[26,27] It is possible to generate hot spots, at the gaps between the nanoparticle aggregates, which have high SERS enhancement.[27–29] However, problems with poor reproducibility of "hot" SERS-active nanostructures, the lack of quantitative SERS signals and the generation of a narrow distribution of high EF values remain

[a]School of Science, MOE Key Laboratory for Nonequilibrium Synthesis and Modulation of Condensed Matter, Xi'an Jiaotong University, Shann Xi, 710049, People's Republic of China. E-mail: hjyou@mail.xjtu.edu.cn; jxfang@mail.xjtu.edu.cn

[b]Institute of Physics, Chinese Academy of Sciences, Beijing, 100090, People's Republic of China

† Electronic supplementary information (ESI) available. See DOI: 10.1039/c3tc30824c

‡ These authors contributed equally to this work.

unresolved.[5,30] By decreasing the size of the Au or Ag nanoparticles, the density of the gaps between the nanoparticles in a certain area can be increased; however, efficient SERS cannot be generated due to the small scattering cross-sections. So far, only Au nanoparticles larger than 20 nm have sufficient plasmonic activity and provide the required SERS enhancement.[5,31,32]

Recently, to obtain both high sensitivity and reproducibility, some progress have been made for the fabrication of SERS substrates using nanoparticle colloids. A typical strategy has involved nanogaps and protrusions, among others, being built on the nanoparticle surface. For example, uniform small gaps with a 1 nm size were constructed on Au nanoparticles, and the single-particle SERS had an enhancement greater than 10^8.[33] Similarly, the protrusions on the metal particle surface will also excite local electromagnetic enhancement on their tips, and thus generate enhanced SERS "hot spots", which can be attributed to the lightning rod effect.[22,34] A series of Ag or Au mesoparticles with various protrusions on the surface have been synthesized and their SERS analysis revealed that they had enhancement factors greater than 10^7, such as sea urchin-like,[12,35] flower-like,[12,22] meatball-like,[10,12] and star-like mesoparticles.[12,15] The nanostructured protrusions on the mesoparticle surface serve as nano-lightning rods, dramatically increasing the excitation cross-section and the electromagnetic field enhancements of the tip plasmons.[36] Thus, the SERS and optical properties of the hierarchical mesoparticle are strongly dependent on the topographies of the mesoparticle surface. Although various mesoparticles with different protrusions on the surface have been synthesized and studied as possible SERS substrates, the influence of the topography on the SERS enhancement has not yet been systematically investigated in detail, mainly due to the absence of a synthesis system to control the surface morphologies of the mesoparticles. Here, a series of Au mesoparticles with meatball-like, urchin-like, and flower-like shapes were obtained in a simple and facile colloid synthesis system. Precise control can be exerted on the surface topologies of the Au mesoparticles when dopa molecules are used to tune the growth behavior of Au nanocrystals. These Au mesoparticles could serve as an ideal target for a systematic investigation of the SERS properties. Using finite-difference time-domain (FDTD) simulation, the localized electric field on the precisely controlled surface was studied, and then the mechanism of SERS enhancement was discussed.

2 Experimental section

2.1 Synthesis of Au mesosuperstructures

In a typical synthesis of mesosuperstrucutures, 2.0 mL chloroauric acid ($HAuCl_4 \cdot 4H_2O$, 10 mM, Beijing Chemical Co., analytical grade) aqueous solution (ultrapure water was used as solvent) was mixed with 6.0 mL water in a 25 mL glass vial by a rotating magnetic bar with a speed of 300 rpm. Then, 2.0 mL dopa (3,4-dihydroxyphenylalanine, 10 mM, Alfa-Aesar, 90%) was added into the glass vial. The color of the mixed solution changed from light yellow to coral immediately. The solutions before mixing were all kept at 10 °C. After 20 min, a coral colored suspension containing Au particles was formed. The suspension was centrifuged at 5000 rpm for 2 min to collect the product that was then washed three times with deionized water.

2.2 Characterization

The morphology of the products was investigated by field emission scanning electron microscopy (FE-SEM) using a JEOL (JSM-7000F) at an accelerating voltage of 20 kV. The transmission electron microscopy (TEM) and high resolution TEM (HRTEM) images as well as selected-area electron diffraction (SAED) pattern images were obtained on a JEOL JEM-2100 transmission electron microscope operating at an accelerating voltage of 200 kV. SERS measurements were carried out on a confocal microprobe Raman spectrometer (LabRAM HR800, HORIBA JOBIN YVON) with 633 nm He–Ne laser line at room temperature. The signal collection time was 1 s with a 850 nm diameter probe area. The incident power of the laser at the samples was 0.055 mW after it was decreased by a D2 attenuation piece. The products of the Au mesoparticles were transferred onto a cleaned quartz plate (0.7 mm × 0.7 mm) as a SERS sample. The samples were prepared by drop casting 50 μL of 1×10^{-7} M crystal violet (CV) aqueous solution on the quartz plate and allowing the solvent to evaporate.

3 Results and discussion

3.1 Controllable surface topographies of gold mesoparticles

As recently reported in a study, $HAuCl_4$ can be reduced by dopa in aqueous solution at room temperature.[37,38] Here, we decreased the reaction temperature to 10 °C for obtaining uniform Au mesoparticles with highly roughened topography. Fig. 1a shows a typical SEM image of Au mesoparticles synthesized with 2.5 mM $HAuCl_4$ and 2.5 mM dopa. These flower-like Au mesoparticles are uniform in both size and morphology. The average size is around 820 nm, a little larger than the sea urchin-like Au mesoparticles (700 nm) synthesized in our previous work using the galvanic replacement method.[35] It can be seen from the SEM image that blade-like petals closely cover the surfaces of the flower-like mesoparticles. As shown in Fig. 1b, the surface topography of the mesoparticles can be controllably tuned by changing the concentrations of the $HAuCl_4$ and dopa. Keeping the concentration ratio between the $HAuCl_4$ and dopa at 1 : 1, the images of S1 to S8 in Fig. 1b show the single-particle morphologies of Au mesoparticles synthesized with $HAuCl_4$ and dopa as the concentration increases from 0.5 mM to 7.0 mM. These mesoparticles are uniform in both size and shape (as shown in Fig. S1†) with a series of regular transformations of the morphologies being formed. At the lower $HAuCl_4$ and dopa concentration (0.5 mM), a meatball-like mesoparticle (S1 in Fig. 1b) is formed with a surface topography of small nanoparticle aggregates (S1-m in Fig. 1c). With the increase of $HAuCl_4$ and dopa concentrations, the size of the building nanoparticles on the surface increases and some tips grow into spikes (S2-m and S3-m in Fig. 1c). The mesoparticles are transformed into an urchin-like shape. When the concentration increases to more than 2.0 mM, the spikes further grow into blade-like shapes (S4 in Fig. 1b). The mesoparticles are

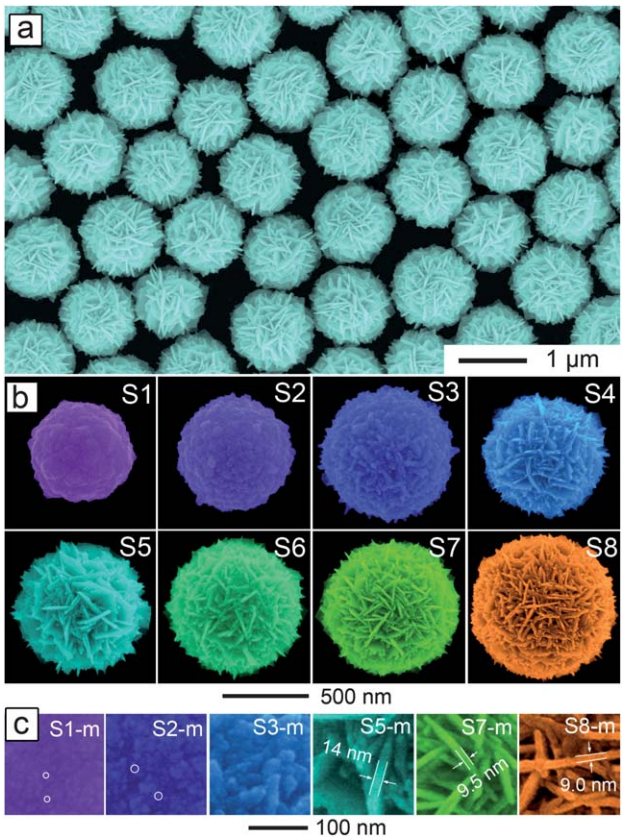

Fig. 1 SEM images of Au mesosuperstructures with controllable surface topographies. (a) Large area Au mesoparticles synthesized under typical conditions (concentration ratio of dopa and $HAuCl_4$ is 2.5 mM/2.5 mM). (b) Surface topography transformation with the change in concentration of dopa/$HAuCl_4$: S1, 0.5 mM/0.5 mM; S2, 1.0 mM/1.0 mM; S3, 1.5 mM/1.5 mM; S4, 2.0 mM/2.0 mM; S5, 2.5 mM/2.5 mM; S6, 3.0 mM/3.0 mM; S7, 4.0 mM/4.0 mM; and S8, 7.0 mM/7.0 mM. (c) Magnification images of surface topographies of samples S1, S2, S3, S5, S7, and S8 shown in (b).

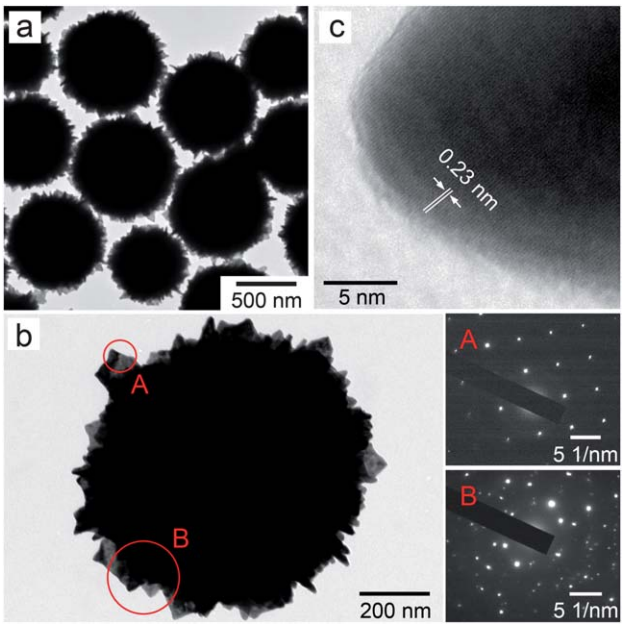

Fig. 2 (a) TEM image of Au mesosuperstructures. (b) TEM image of a single Au mesosuperstructure and the SAED patterns obtained from the 'A' and 'B' circled areas. (c) HRTEM image of a petal on the flower-like Au mesosuperstructure.

transformed into a flower-like shape with blade-like petals closely covering the surface. As the concentration increases, the blades on the surface become thinner, ranging from 14 nm to 9 nm (S5-m to S8-m in Fig. 1c). At the same time, the density of the petals increases, and the width of the slits formed between petals decreases accordingly.

Fig. 2a shows the TEM images of the typical Au mesoparticles synthesized with 2.5 mM $HAuCl_4$ and dopa. From the TEM image, it can be seen that the surfaces of the uniform mesoparticles are covered by petals, as has been shown previously in the SEM images. The SAED patterns in Fig. 2b indicate that each petal is a single-crystal structure and their crystalline directions are arranged differently on the mesocrystal surface. The HRTEM image in Fig. 2c further shows the single-crystal structure of a single petal. The lattice space is 0.23 nm, which matches with Au (111) plane *d*-spacing (0.235 nm).

3.2 Mechanism of the topography transformation

The formation process of the typical flower-like Au mesoparticles was studied by analyzing the samples taken from the reaction mixture after different reaction periods using the SEM. As shown in Fig. 3a, the sample obtained just after the reaction has started (around 5 s) presents particles with a size of around 100 nm and a rough surface. When the reaction time was increased to 1 min, the particles' morphology remained the same but the size increased to around 500 nm (Fig. 3b). With further increase in the reaction time, the tips on the particle's

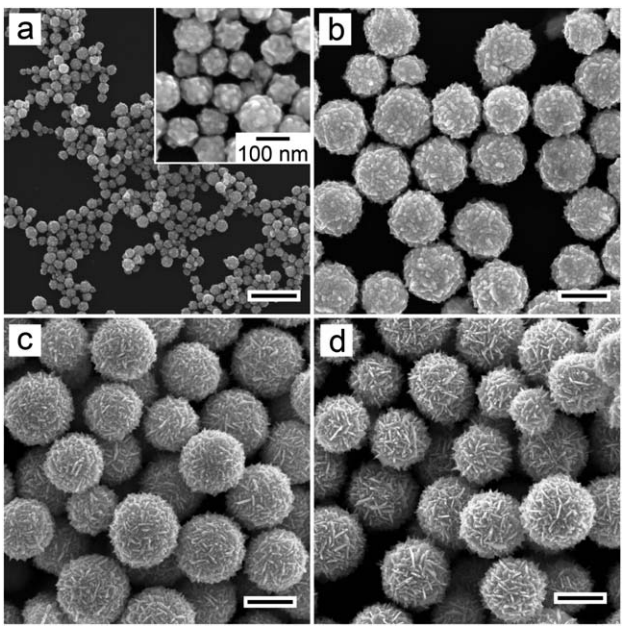

Fig. 3 SEM images of Au mesosuperstructures synthesized at different reaction times: (a) 5 s, (b) 1 min, (c) 3.5 min, and (d) 10 min. The scale bars are 500 nm.

rough surface gradually grew into blade-like petals (Fig. 3c and d). Finally, uniform mesoparticles with a flower-like shape were formed.

In the synthesis system, there were only three components: water, $HAuCl_4$ and dopa. The water only acted as a solvent. In the reaction, the Au^{3+} ions were reduced by dopa.[37,38] At the same time, dopa also acted as a surfactant to stabilize the Au colloid particles.[37] Our previous density functional theory (DFT) calculation results indicated that the amine and carboxylic acid functional groups on the top of the dopa molecules will be adsorbed on the Au particle surface.[39] As shown in Fig. 4a, there are two oxhydryl groups at the bottom part of the dopa molecule. The molecular dynamic (MD) simulation result (Fig. 4b and c) shows that the oxhydryl groups on different dopa molecules will interact with each other to form hydrogen bonds between them when these dopa molecules are close to each other. The interaction energy due to the formation of two hydrogen bonds between two dopa molecules is 0.407 eV (energy of each bond is 0.203 eV, details of the calculation are presented in the ESI†), which is larger than the thermal dynamic energy of the molecules ($E_v \sim k_BT = 0.026$ eV). This indicates that when the top parts of the dopa molecules are adsorbed on the particle surface, their bottom parts will aggregate with each other.

Based on the information from Fig. 3 and 4, the growth process of an Au mesoparticle as presented in Fig. 5 is suggested and illustrated. As shown in Fig. 5a, small Au nanoparticles are first formed, and are stabilized with dopa molecules, on the surface as capping agents. The bottom parts of the dopa molecules aggregate with each other and "glue" the small Au nanoparticles together, due to hydrogen bond formation (Fig. 5b). Under the function of this "glue" effect of the dopa molecules, the small Au nanoparticles will aggregate together to form mesoparticles with a rough surface. As shown in Fig. 5c, the aggregation of the dopa molecule bottom parts will leave space on the top parts of the humps on the rough surface, allowing Au atoms/ions to be deposited on the hump tips. Thus, under the directional function of the dopa molecules, the tips will gradually grow into blade-like petals, as shown in Fig. 5d. In total, in the formation process of the Au mesoparticle, the dopa molecules have three functions. Firstly, they act as a reducing agent to reduce the Au ions. Secondly, they act as capping agents to stabilize the Au nanoparticle and "glue" them to the aggregate. Thirdly, the dopa capping agents can direct the Au ions to be preferentially absorbed on the tips of the rough surface, leading to a protuberant growth on the gold mesoparticle surface with higher curvature.[40] The second and third roles of the dopa molecules are very similar to that of the CTAB.[12]

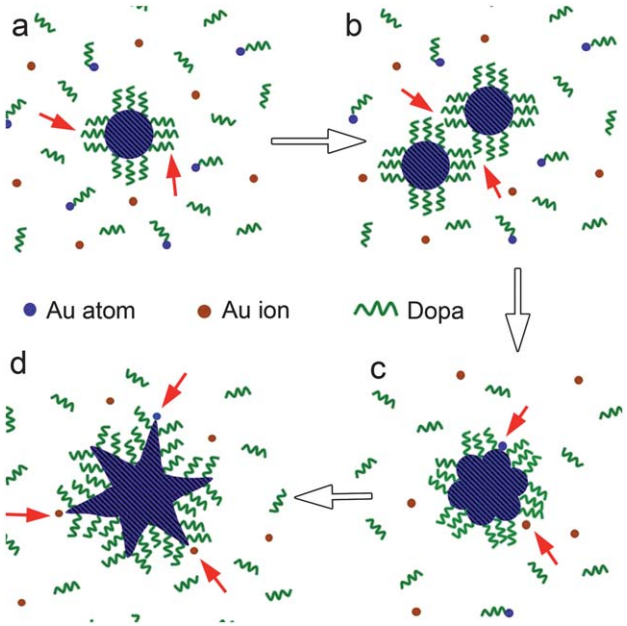

Fig. 5 Schematic illustration of the growth process of an Au mesoparticle. (a) The first step shows the formation of small Au nanoparticles that are stabilized by dopa molecules. (b) The second step shows the aggregation of the small Au nanoparticles with the help of the "glue" function of the dopa molecules. (c and d) Dopa ligand directed Au ions or atoms absorbed on the tips of the rough surface, leading to a protuberant growth.

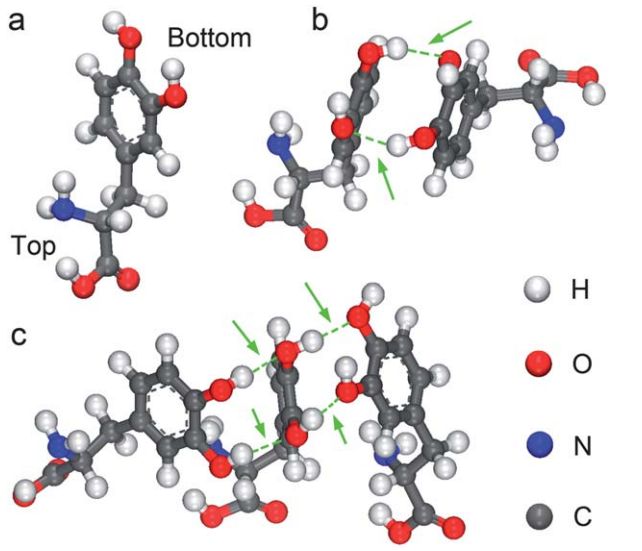

Fig. 4 MD simulation result of the configurations of dopa molecules. (a) Single dopa molecule. (b) Two and (c) three bottom aggregated dopa molecules. The arrows indicate the hydrogen bonds.

Similar to Xie's and our previous reports,[35,41] a Lamer curve is used to explain the growth process of the Au mesoparticle. As shown in Fig. 6a, four steps are involved in the growth process of the hierarchical three-dimensional (3D) structure. In the first step, as the Au ions are reduced by the dopa, the concentration of the Au atoms increases gradually. In the second step, when the concentration of Au atoms exceeds the supersaturation point of nucleation, the atoms will aggregate to form a stable nucleus. At the same time, the nucleus will grow with more Au atoms being added to it. Thus, a great number of Au nanoparticles are obtained in the solution. These first two steps are the same as the classical growth of colloid metal particles.[42] Following them, the nanoparticles will aggregate to form mesoparticles with the help of the "glue" function of the dopa. This

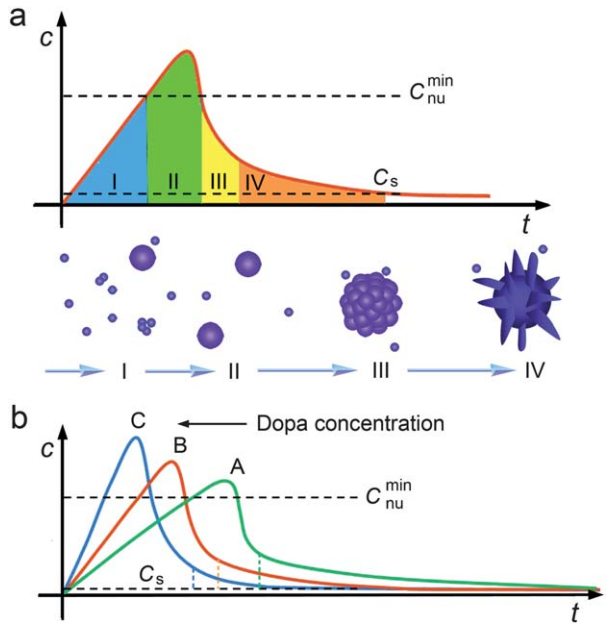

Fig. 6 (a) Schematic plot of Au atom concentration (c) *versus* time (*t*) illustrating the growth process of Au mesoparticles (Lamer curve). (b) Dopa concentration effect on the plot transformation (Lamer curves from A to C).

process belongs to a new non-classical crystal growth, which is called "particle-mediated growth".[12,43,44] Through particle-mediated growth, the polycrystalline or mesocrystal structures can be formed depending on the growth conditions.[12,43–46] In this case, polycrystalline mesoparticles are obtained, as the SAED pattern shown in Fig. 2b. The particle aggregation depends on the density (ρ) of the nanoparticles, as the equation of aggregation frequency (f) describes:[39]

$$f = kT\rho^{2/3}/3\pi\eta r \quad (1)$$

where r is the radius of the particle, T and η are the temperature and viscosity of the solution, and k is the Boltzmann constant. With the density of the particle units (ρ) decreasing and the size of the particle-aggregated mesoparticles (r) increasing, the particle-mediated growth will finally be suspended due to the aggregation frequency (f) decreasing to a very low level. Depending on eqn (1), large mesoparticles will grow more slowly through particle-mediated growth than small mesoparticles, because large mesoparticles have a lower aggregation frequency. Thus, Au mesoparticles with a uniform size will be formed in the third step through particle-mediated growth. From eqn (1), it is possible to obtain the average size of the uniform mesoparticles as:

$$r = kT\rho^{2/3}/3\pi\eta f_m \quad (2)$$

where f_m is the suspending aggregation frequency. This equation indicates that larger mesoparticles will be obtained with a larger density of particle units (ρ). An example is shown in Fig. 3a and b. In the last step, the remaining Au ions and atoms will be deposited on the surface tips of the Au mesoparticles under the directional function of the dopa capping agents to form a protuberant growth on the gold mesoparticle surface.[47]

Based on the growth process described in Fig. 6a, the morphology of the Au mesoparticles can be tuned by changing the Lamer curve. As shown in Fig. 6b, as the dopa concentration increases, the plot of the Au atom concentration will transform from A to C. Fig. 7 shows the SEM images of Au mesoparticles synthesized with different dopa concentrations. As a reducing agent, the increase of the dopa concentration will speed up the reduction reaction of the Au ions. Thus, more Au atoms will be produced in the first step with the increase of dopa concentration. Following this, more Au nanoparticles will be produced in the second step, resulting in the formation of a larger mesoparticle based on eqn (2). As shown in Fig. 7a–f, the base spherical radius of the mesoparticles increases continually with the increase of dopa concentration. On the other hand, in the situation where more Au ions are reduced in the first and second steps, there will be less support for the growth of tips on the mesoparticle surface in the fourth step, as there will be fewer remaining Au ions (as shown by dotted lines in Fig. 6b). Thus, the size of the mesoparticle petals will decrease as the dopa concentration increases, as shown in Fig. 7a–f. The petals even disappear when the dopa concentration increases to 3.5 mM (Fig. 7f).

In addition to the concentrations of dopa and $HAuCl_4$, the temperature of the synthesis also has an important effect on the morphology of the mesoparticles. As shown in Fig. 8 and S2,† the Au mesoparticles transformed from the flower-like to meatball-like shapes when the temperature increased from 0 °C to 40 °C. At the same time, the size of the mesoparticles decreases accordingly, as shown in Fig. 8f. The higher temperature will speed up the reaction and activate the deposited Au

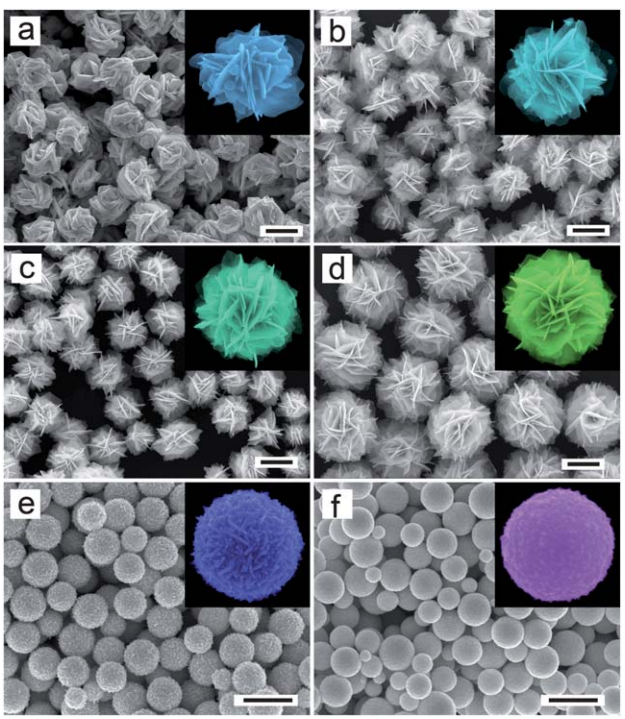

Fig. 7 SEM images of Au mesoparticles synthesized with 2.5 mM $HAuCl_4$ and different dopa concentrations: (a) 0.5 mM, (b) 1.0 mM, (c) 1.5 mM, (d) 2.0 mM, (e) 3.0 mM, and (f) 3.5 mM. The scale bars are 1 μm.

atoms to more easily diffuse on the mesoparticle surface.[39] The anisotropic growth of the tips will be eliminated by the free diffusion of Au atoms at higher temperatures.[43] Thus, the sharp blade-like petals will disappear at higher temperatures.

The experimental and growth mechanism studies indicate that the topography of the Au mesoparticles can be precisely controlled in this particle-mediated growth system by changing the synthesis conditions, including the shape and size of the nanotextured tips on the surface. In the previous study, only the Au flower-like particle was synthesized under certain synthesis conditions and there has been no report on precise control of surface morphologies. For example, in the Au flower-like particles reported by Jia and Lee groups,[41,48] only the particle size can be tuned by changing the synthesis conditions, and the control for the surface shape has not been studied.

3.3 SERS properties

The SERS properties of individual Au mesoparticles with different topographies were evaluated using crystal violet (CV), a well-known SERS analyte. Due to complex plasmonic patterns in relatively large and textured Au particles, even a single particle can potentially be an efficient single particle SERS (sp-SERS) "substrate" with multiple and bright "hot spots". For the measurement of individual mesoparticles, silicon wafers coated with mesoparticles were used. As shown in Fig. S3,† the separated individual Au mesoparticles were selected for the sp-SERS measurement. Fig. 9 shows the typical SERS spectra of CV adsorbed on individual Au mesoparticles with different morphologies noted as S1, S2, S3, S4, S5, and S8 correlated with the samples shown in Fig. 1b. As previously shown in Fig. 1b, the sample S1 is a meatball-like particle, the samples S2 and S3 are urchin-like particles, and the samples S4–S8 are flower-like particles with decreased petal size and increased petal density. To simplify the SERS result, the samples S6 and S7 were omitted for the SERS and S4, S5 and S8 were selected as the representative for the flower-like particles. The SERS spectra reveal the characteristic peaks of CV, for instance, at 1172, 1371, and 1619 cm^{-1}, and correspond well to the ordinary Raman spectra

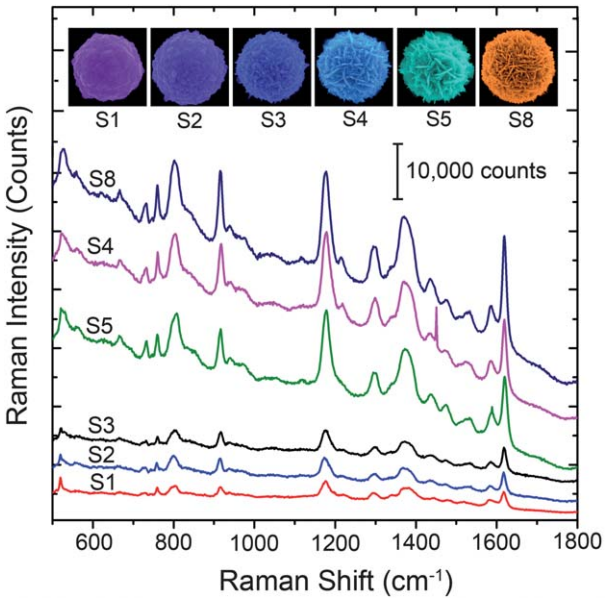

Fig. 9 SERS properties of gold mesoparticles with different surface topographies.

of CV in the solid state and in aqueous solution. The SERS properties of the samples were evaluated from the enhancement factors (EFs), which were estimated by following the procedures and assumptions described in previous reports (for details see ESI†).[49,50] There was an apparent trend, namely, as the surface texture increased, the EFs of the SERS intensity increased. The estimated average EFs of a single mesoparticle for the six samples were: S1, 1.12×10^7; S2, 2.06×10^7; S3, 2.85×10^7; S4, 7.82×10^7; S5, 8.56×10^7; and S8, 1.07×10^8. These results are consistent with previous reports, such as the EFs of Au meatball-like mesoparticles, which are 10^6 to 10^7 and 10^6 in Wang's and in our previous reports, respectively. Depending on the Xu group report, the highly branched structures on Au flower-like mesoparticles are supposed to be rich in hot spots, thus giving strong SERS signals.[51]

As previously discussed, in the synthesis process, the Au mesostructures are stabilized by dopa molecules. There is an aromatic ring both in the dopa and CV molecules, which contributed to most SERS signal peaks.[52,53] In order to evaluate the effect of the residual dopa ligand on the SERS intensity, the SERS of Au mesoparticles without CV doping was measured, as shown in Fig. S4.† The SERS signal peaks of the blank Au mesoparticles (sample S5) are very weak and randomly distributed, which cannot match with Raman scattering of dopa or CV molecules. This result indicates that the residual dopa may be oxidized by oxygen under the catalytic action of the rough Au mesoparticle surface, similar to aerobic oxidation reactions catalysed by Au nanoparticles.[54,55] Thus, in this work, the residual dopa ligand has no obvious effect on the SERS intensity of Au mesoparticles.

The reproducibility of the SERS signal on different individual Au flower-like mesoparticles (sample S5) also was investigated. Fig. 10a and b demonstrate the 3D waterfall plot and intensity map of the sp-SERS spectra obtained from 18 separated

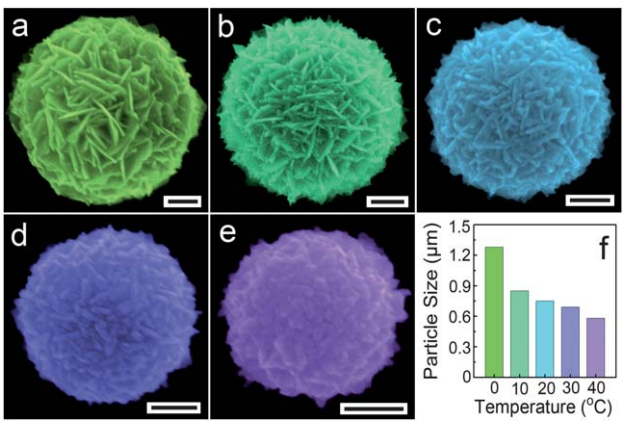

Fig. 8 (a–e) SEM images and (f) size transformation of Au mesoparticles synthesized at different temperatures: (a) 0 °C, (b) 10 °C, (c) 20 °C, (d) 30 °C, and (e) 40 °C. The scale bars are 500 nm.

individual mesoparticles, displaying uniform Raman intensity of CV peaks at 1172, 1371, and 1619 cm^{-1}. The deviations of the Raman intensity are less than 30% for most particles, except for no. 2, 5, and 9 particles. In this study, the size of Au mesoparticles (820 nm) is close to the laser spot diameter (850 nm). Thus the reproducibility of sp-SERS would be greatly decreased by the misalignment between the centres of the laser spot and the Au mesoparticle during the actual measurement (Fig. S5†). The same particle was measured 5 times (Fig. S6†), indicating that the misalignment between the particle and laser spot would induce 20% deviation for the reproducibility. After deducting this 20% deviation induced by misalignment, the actual deviation of the SERS signal on the Au mesoparticles is only about 10–15%.

To corroborate the observed relationship between the SERS activities and surface topographies of the Au mesoparticles, a FDTD simulation was performed to obtain the distribution of local electric field intensity around the model Au mesoparticles with monochromatic light at 532, 632, and 785 nm. It is generally agreed that the Raman intensity increases by a factor $|E|^4$ with respect to the local electric field on the SERS substrate surface.[56] Based on the SERS samples, six simplified simulation models (A–F) with various nanotextured topographies on the Au mesoparticle surfaces were built to obtain the localized electric field, as shown in Fig. 11. The geometrical details of the models are described in the ESI.† The right-hand panels in Fig. 11a–f show the typical distribution of the electric field strength $|E|$ calculated in the x–y plane (the z–x plane is shown in Fig. S7†) across the vertical axes of these model mesoparticles irradiated with monochromatic light from top to bottom along the z axis at 632 nm. Model A, a smooth sphere as a contrast model, has the weakest E-field amplitude distribution. In model B for the meatball-like particle, the localized electric field is excited by the nanoprotrusions on the surface, as they act like nano-lightning rod. However, the excitation for the strong localized electric field is suppressed by the lower curvature of the protrusions and the large spherical surface on the mesoparticle. In model C, the localized electric field is excited at the junctions of the blade-like petals with the sphere surface, but due to the size of the petals, with lower height and shorter length, they could not effectively confine the light in cavity between the petals. From models D to F, with density, height, and length of the petals increasing, the light can be more effectively confined in the cavity between the petals, resulting in a stronger localized electric field being excited on the tips of the petals and slits between them by the confined light. Thus, the local electric field is enhanced by two kinds of topography structures. One is the vicinity of the blade-like tips with high curvature that acts as nano-lightning rod enhancement and the other is the slit area between two petals that acts as nanogap enhancement.

Depending on the maximal $|E|$ enhancement, the models can be separated into three groups: model A, models B and C, and models D–F, with a maximal $|E|$ being around 2–3, 10–12 and 50–60 N/C, respectively. More obvious enhancement is exhibited by the second group of models, than the first group, as they have a rougher surface. The well textured topographies with blade-like petals covering the surface in the third group of models further promote the enhancement of the local electric field intensity. In the third group, the maximal $|E|$ for models D, E, and F is similar; however, the number and density of "hot spots" with maximal $|E|$ obviously increase along the sequence of models from D to F, as shown in Fig. 11d–f and S7d–f.† This is due to the increase in the number of blade-like petal tips and the slits formed between petals on the mesoparticle surface.

It is well-known that the SERS property can be optimized when the excitation light wavelength matches the plasmonic

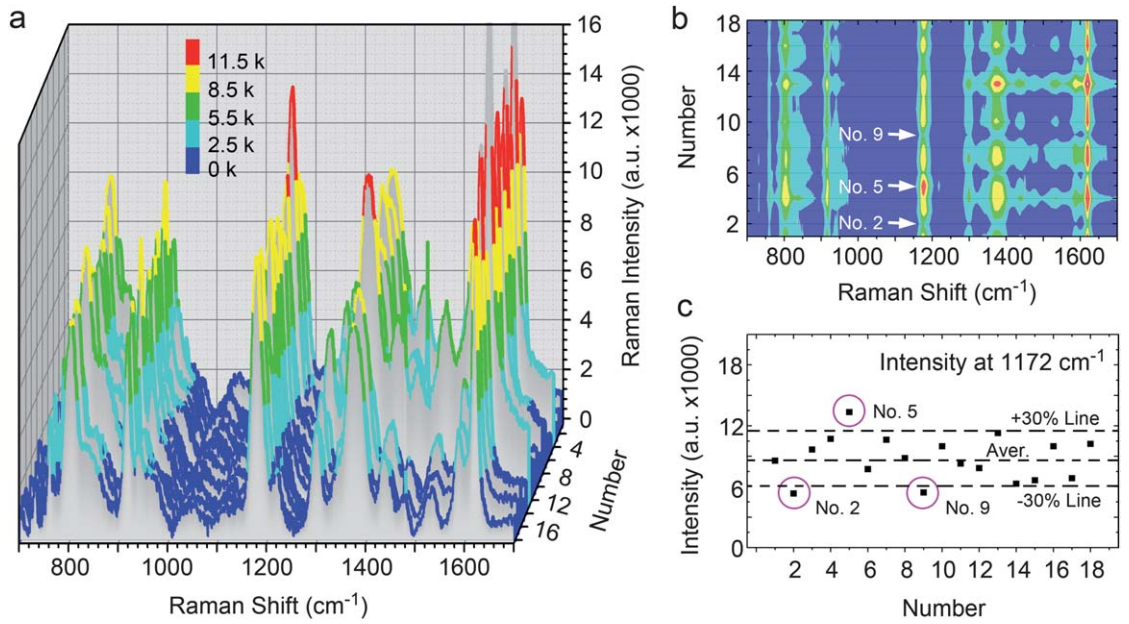

Fig. 10 (a) Raman spectra obtained from 18 separated individual Au flower-like mesoparticles (sample S5). The correlated (b) intensity map and (c) intensity deviation at 1172 cm^{-1}.

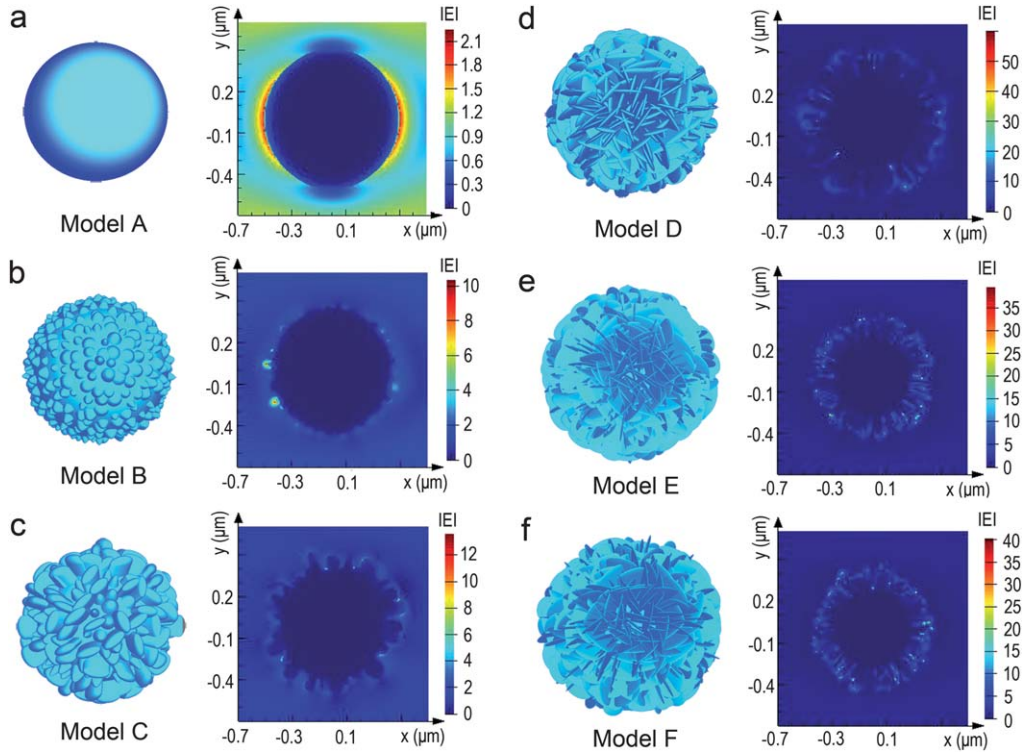

Fig. 11 E-field amplitude patterns in the *x*–*y* plane from FDTD theoretical simulation at the excitation electromagnetic wavelength of 633 nm for (a–f) six mesoparticle models with different topographies.

resonance of the metal nanostructure.[15] The FDTD simulation with irradiated light at different wavelengths indicated that the effect of the excitation wavelength on the SERS was highly dependent on the textured topographies of the mesoparticles. This is illustrated in the histograms of maximal electric field calculated for models A–F irradiated at 532, 632, and 785 nm (Fig. 12). For the models A–D, the dependence of the SERS effect on the excitation wavelength is not obvious. However, for the models E to F, the dependence becomes especially strong for their highly textured topographies. The ratio of maximal electric field strength irradiated at 532 and 785 nm increases by 1.3, 1.8, to 3.9 for models D, E, to F, respectively, in the *x*–*y* plane (by 1.2, 2.3, to 2.8 in *z*–*y* plane, respectively). This indicates that the light with longer wavelength are more easily confined in the more highly nanotextured surface, such as that of the model F which has the highest curvature and density of the blade-like tips. On the other hand, near the surface area, the local electric field strength is stronger than that in the middle cross-plane, such as the distribution of the electric field in the plane parallel to the *x*–*y* plane at $z = 0.35$ μm, as shown in Fig. S8.† In this plane, same as

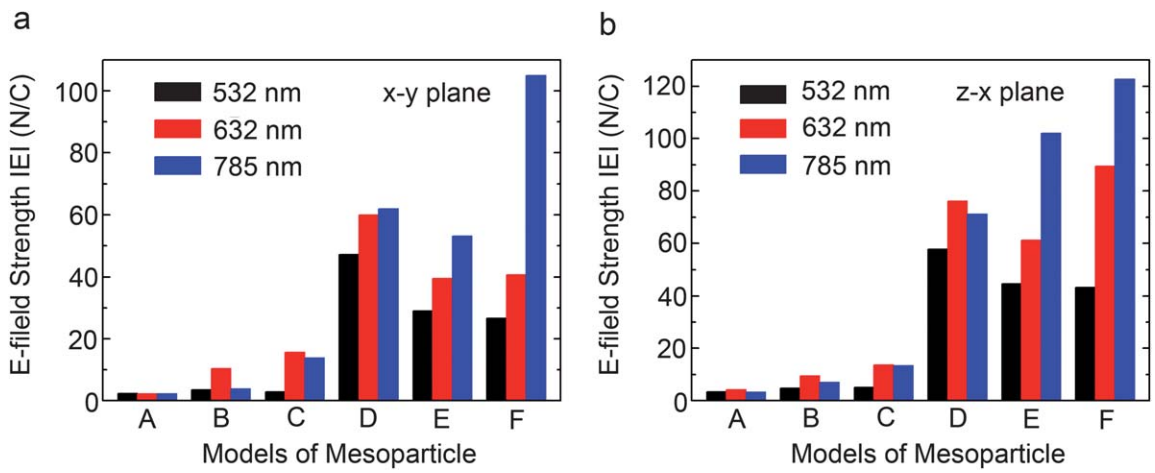

Fig. 12 Histograms of maximal electric field enhancements calculated from models A–F at excitation wavelengths of 532, 632, and 785 nm from (a) *x*–*y* and (b) *z*–*x* planes.

the *x*–*y* plane, the number and density of "hot spots" also increase accordingly following the sequence of model D to F.

4 Conclusions

In summary, using a facile nanoparticle-mediated growth protocol, Au mesoparticles with controllable morphologies have been synthesized as an ideal target for a systematic investigation of the SERS property. Several advantages have been revealed. Firstly, this colloid synthesis system is very simple, just consisting of three components, but very versatile, where a series of Au mesoparticles, including meatball-like, urchin-like, and flower-like shapes, can be obtained. At the same time, the surface topography of the Au mesoparticles can be accurately tailored by the three functions of the dopa molecules. The three roles of the dopa molecules are: as a reducing agent, as a "glue" that promotes nanoparticle unit aggregation, and as a direction agent for metal crystal anisotropic growth with high curvature on the surface. Secondly, the highly textured topography can obviously improve the SERS properties. The flower-like mesoparticles with highly crowded blade-like petals on the surface exhibit a higher enhancement of SERS than the meatball-like and urchin-like mesoparticles. The FDTD simulation for six models irradiated at different wavelengths indicated that the closely covered petals on the mesoparticle surface could effectively confine light in the cavities between the petals. The confined light will inspire strong enhancement of the electric field at the tips of the petals and slits between the petals due to the nano-lightning rod and nanogap effects. The higher density of the petals on the mesoparticle can produce more "hot spots" with an enhanced local electric field on the highly textured topography. Our studies are expected to help people deeply understand not only the particle-mediated growth process for the formation of various types of mesostructures but also the interaction between light and plasmons in these structures at the nanoscale. These well-defined Au flower-like mesoparticles hold great promise for ultrasensitive detection by SERS and are expected to find a range of applications in fields such as life sciences, environmental science, and photonics.

Acknowledgements

This work was supported by Natural Science Foundation of Shaanxi Province (Grant no. 2012JQ6006), National Natural Science Foundation of China (Grant nos. 51171139 and 51201122), Doctoral Fund for New Teachers (nos. 20120201120049 and 20110201120039), Tengfei Talent Project of Xi'an Jiaotong University, New Century Excellent Talents in University (NCET), Scientific New Star Program in Shaanxi Province (no. 2012KJXX-03) and Fundamental Research Funds for the Central Universities.

Notes and references

1 J. F. Li, Y. F. Huang, Y. Ding, Z. L. Yang, S. B. Li, X. S. Zhou, F. R. Fan, W. Zhang, Z. Y. Zhou, D. Y. Wu, B. Ren, Z. L. Wang and Z. Q. Tian, *Nature*, 2010, **464**, 392–395.
2 Y. W. C. Cao, R. C. Jin and C. A. Mirkin, *Science*, 2002, **297**, 1536–1540.
3 X. M. Qian and S. M. Nie, *Chem. Soc. Rev.*, 2008, **37**, 912–920.
4 E. J. Smythe, M. D. Dickey, J. M. Bao, G. M. Whitesides and F. Capasso, *Nano Lett.*, 2009, **9**, 1132–1138.
5 S. E. J. Bell and N. M. S. Sirimuthu, *Chem. Soc. Rev.*, 2008, **37**, 1012–1024.
6 M. Fleischm, P. J. Hendra and A. J. McQuilla, *Chem. Phys. Lett.*, 1974, **26**, 163–166.
7 W. Kubo and S. Fujikawa, *Nano Lett.*, 2011, **11**, 8–15.
8 D. He, B. Hu, Q. F. Yao, K. Wang and S. H. Yu, *ACS Nano*, 2009, **3**, 3993–4002.
9 S. K. Yang, F. Xu, S. Ostendorp, G. Wilde, H. Zhao and Y. Lei, *Adv. Funct. Mater.*, 2011, **21**, 2446–2455.
10 H. Wang and N. J. Halas, *Adv. Mater.*, 2008, **20**, 820–825.
11 J. X. Fang, S. Y. Liu and Z. Y. Li, *Biomaterials*, 2011, **32**, 4877–4884.
12 H. J. You, Y. T. Ji, L. Wang, S. C. Yang, Z. M. Yang, J. X. Fang, X. P. Song and B. J. Ding, *J. Mater. Chem.*, 2012, **22**, 1998–2006.
13 J. X. Fang, S. Lebedkin, S. C. Yang and H. Hahn, *Chem. Commun.*, 2011, **47**, 5157–5159.
14 H. X. Xu, J. Aizpurua, M. Kall and P. Apell, *Phys. Rev. E: Stat. Phys., Plasmas, Fluids, Relat. Interdiscip. Top.*, 2000, **62**, 4318–4324.
15 M. J. Mulvihill, X. Y. Ling, J. Henzie and P. D. Yang, *J. Am. Chem. Soc.*, 2010, **132**, 268–274.
16 Z.-Y. Li and Y. Xia, *Nano Lett.*, 2010, **10**, 243–249.
17 M. Rycenga, X. H. Xia, C. H. Moran, F. Zhou, D. Qin, Z. Y. Li and Y. A. Xia, *Angew. Chem., Int. Ed.*, 2011, **50**, 5473–5477.
18 C. F. Tian, C. H. Ding, S. Y. Liu, S. C. Yang, X. P. Song, B. J. Ding, Z. Y. Li and J. X. Fang, *ACS Nano*, 2011, **5**, 9442–9449.
19 H. Wang, C. S. Levin and N. J. Halas, *J. Am. Chem. Soc.*, 2005, **127**, 14992–14993.
20 C. Tabor, R. Murali, M. Mahmoud and M. A. El-Sayed, *J. Phys. Chem. A*, 2009, **113**, 1946–1953.
21 P. G. Etchegoin, C. Galloway and E. C. Le Ru, *Phys. Chem. Chem. Phys.*, 2006, **8**, 2624–2628.
22 H. Y. Liang, Z. P. Li, W. Z. Wang, Y. S. Wu and H. X. Xu, *Adv. Mater.*, 2009, **21**, 4614–4618.
23 J. X. Fang, H. J. You, B. J. Ding and X. P. Song, *Electrochem. Commun.*, 2007, **9**, 2423–2427.
24 C. F. Tian, Z. Liu, J. H. Jin, S. Lebedkin, C. Huang, H. J. You, R. Liu, L. Q. Wang, X. P. Song, B. J. Ding, M. Barczewski, T. Schimmel and J. X. Fang, *Nanotechnology*, 2012, **23**, 165604.
25 C. L. Haynes, A. D. McFarland and R. P. Van Duyne, *Anal. Chem.*, 2005, **77**, 338a–346a.
26 F. Le, D. W. Brandl, Y. A. Urzhumov, H. Wang, J. Kundu, N. J. Halas, J. Aizpurua and P. Nordlander, *ACS Nano*, 2008, **2**, 707–718.
27 D. Graham, D. G. Thompson, W. E. Smith and K. Faulds, *Nat. Nanotechnol.*, 2008, **3**, 548–551.
28 W. Y. Li, P. H. C. Camargo, X. M. Lu and Y. N. Xia, *Nano Lett.*, 2009, **9**, 485–490.

29 J. P. Camden, J. A. Dieringer, Y. M. Wang, D. J. Masiello, L. D. Marks, G. C. Schatz and R. P. Van Duyne, *J. Am. Chem. Soc.*, 2008, **130**, 12616–12617.
30 Y. Fang, N. H. Seong and D. D. Dlott, *Science*, 2008, **321**, 388–392.
31 W. Xie, B. Walkenfort and S. Schlucker, *J. Am. Chem. Soc.*, 2013, **135**, 1657–1660.
32 J. T. Krug, G. D. Wang, S. R. Emory and S. Nie, *J. Am. Chem. Soc.*, 1999, **121**, 9208–9214.
33 J. M. Nam, D. K. Lim, K. S. Jeon, J. H. Hwang, H. Kim, S. Kwon and Y. D. Suh, *Nat. Nanotechnol.*, 2011, **6**, 452–460.
34 L. M. Tong, Z. P. Li, T. Zhu, H. X. Xu and Z. F. Liu, *J. Phys. Chem. C*, 2008, **112**, 7119–7123.
35 J. X. Fang, S. Y. Du, S. Lebedkin, Z. Y. Li, R. Kruk, M. Kappes and H. Hahn, *Nano Lett.*, 2010, **10**, 5006–5013.
36 F. Hao, C. L. Nehl, J. H. Hafner and P. Nordlander, *Nano Lett.*, 2007, **7**, 729–732.
37 W. G. Qu, S. M. Wang, Z. J. Hu, T. Y. Cheang, Z. H. Xing, X. J. Zhang and A. W. Xu, *J. Phys. Chem. C*, 2010, **114**, 13010–13016.
38 F. G. Xu, K. Cui, Y. J. Sun, C. L. Guo, Z. L. Liu, Y. Zhang, Y. Shi and Z. A. Li, *Talanta*, 2010, **82**, 1845–1852.
39 Z. M. Peng, H. J. You and H. Yang, *ACS Nano*, 2010, **4**, 1501–1510.
40 J. Perez-Juste, L. M. Liz-Marzan, S. Carnie, D. Y. C. Chan and P. Mulvaney, *Adv. Funct. Mater.*, 2004, **14**, 571–579.
41 J. P. Xie, Q. B. Zhang, J. Y. Lee and D. I. C. Wang, *ACS Nano*, 2008, **2**, 2473–2480.
42 Y. N. Xia, Y. J. Xiong, B. Lim and S. E. Skrabalak, *Angew. Chem., Int. Ed.*, 2009, **48**, 60–103.
43 H. You, S. Yang, B. Ding and H. Yang, *Chem. Soc. Rev.*, 2013, **42**, 2880–2904.
44 J. Fang, B. Ding and H. Gleiter, *Chem. Soc. Rev.*, 2011, **40**, 5347–5360.
45 J. X. Fang, H. J. You, P. Kong, Y. Yi, X. P. Song and B. J. Ding, *Cryst. Growth Des.*, 2007, **7**, 864–867.
46 J. X. Fang, H. J. You, P. Kong, B. J. Ding and X. P. Song, *Appl. Phys. Lett.*, 2008, **92**, 143111.
47 H. J. You, C. H. Ding, X. P. Song, B. J. Ding and J. X. Fang, *CrystEngComm*, 2011, **13**, 4991–4995.
48 D. Xu, J. Gu, W. Wang, X. Yu, K. Xi and X. Jia, *Nanotechnology*, 2010, **21**, 375101.
49 W. B. Cai, B. Ren, X. Q. Li, C. X. She, F. M. Liu, X. W. Cai and Z. Q. Tian, *Surf. Sci.*, 1998, **406**, 9–22.
50 Y. Wang, M. Becker, L. Wang, J. Q. Liu, R. Scholz, J. Peng, U. Gosele, S. Christiansen, D. H. Kim and M. Steinhart, *Nano Lett.*, 2009, **9**, 2384–2389.
51 L. F. Zhang, S. L. Zhong and A. W. Xu, *Angew. Chem., Int. Ed.*, 2013, **52**, 645–649.
52 L. Q. Lu, Y. Zheng, W. G. Qu, H. Q. Yu and A. W. Xu, *J. Mater. Chem.*, 2012, **22**, 20986–20990.
53 W. G. Qu, L. Q. Lu, L. Lin and A. W. Xu, *Nanoscale*, 2012, **4**, 7358–7361.
54 H. Tsunoyama, N. Ichikuni, H. Sakurai and T. Tsukuda, *J. Am. Chem. Soc.*, 2009, **131**, 7086–7093.
55 C. M. Fan, L. F. Zhang, S. S. Wang, D. H. Wang, L. Q. Lu and A. W. Xu, *Nanoscale*, 2012, **4**, 6835–6840.
56 P. Dawson, J. A. Duenas, M. G. Boyle, M. D. Doherty, S. E. J. Bell, A. M. Kern, O. J. F. Martin, A. S. Teh, K. B. K. Teo and W. I. Milne, *Nano Lett.*, 2011, **11**, 365–371.

